J Mater Sci: Mater Electron (2022) 33:12615–12628

Ultra-low thermal conductivity of $AgBiS_2$ via Sb substitution as a scattering center for thermoelectric applications

T. Manimozhi[1], S. Kavirajan[2], K. Kamala Bharathi[1,2], E. Senthil Kumar[1,2], and M. Navaneethan[1,2,*]

[1] *Nanotechnology Research Centre (NRC), SRM Institute of Science and Technology, Kattankulathur, Tamil Nadu 603203, India*
[2] *Functional Materials and Energy Devices Laboratory, Department of Physics and Nanotechnology, SRM Institute of Science and Technology, Kattankulathur, Tamil Nadu 603203, India*

Received: 1 October 2021
Accepted: 5 April 2022
Published online: 16 May 2022

ABSTRACT

$AgBiS_2$ is a promising thermoelectric material, because of its environmentally compatible composition. In this study, a process of the solvothermal method followed by spark plasma sintering was applied to the preparation of $AgBiS_2$ and $AgBi_{1-x}Sb_xS_2$ (x = 0.5–1) materials. The prepared samples were characterized by various techniques. The results revealed the significant and beneficial role of antimony-substituted sample ($AgBi_{0.5}Sb_{0.5}S_2$). The multiphase of $AgSbS_2$ (73.70%), Ag_3SbS_3 (22.59%), and Bi_2S_3 (3.71%) were found by Rietveld refinement technique. The optical properties showed the narrow direct bandgap of ~ 0.83 eV which can be helpful to transport the charge carriers easily. $AgBiS_2$ and $AgBi_{1-x}Sb_xS_2$ (x = 0.5–1) have grain boundaries due to the presence of multiphase in the samples. The numerous interfaces and grain boundaries were known as a disordered arrangement of atoms, which remarkably enhanced the phonon scattering. It leads to low thermal conductivity of 0.21 Wm^{-1} K^{-1} at 333 K in $AgBi_{0.5}Sb_{0.5}S_2$ sample; it has the phases such as cubic-$AgSbS_2$ (73.70%), rhombohedral-Ag_3SbS_3 (22.59%), and orthorhombic-Bi_2S_3 (3.71%). The plausible reason for low thermal conductivity was predicted as the occurrence of phonon scattering mechanism at grain boundaries of the multiphases.

1 Introduction

Due to the increment of energy demand by industrialization, the world must face major problems such as limitation of energy sources, air pollution and global warming [1]. In addition to that, the utilization of energy is 34% from the energy resources, and the remaining (66%) of the energy is wasted in the form of heat that affects the environment. Thermoelectricity (TE) has gained remarkable attention toward researchers owing to the conversion of waste heat energy into useful electrical energy by the

Address correspondence to E-mail: m.navaneethan@gmail.com

https://doi.org/10.1007/s10854-022-08211-y

phenomenon of Seebeck effect. The efficiency of thermoelectric conversion is determined by a dimensionless figure-of-merit $zT = (\sigma S^2 T)/(\kappa_e + \kappa_l)$, where S, σ, T, κ_e and κ_l denote the Seebeck coefficient ($\mu V\ K^{-1}$), electrical conductivity ($S\ cm^{-1}$), absolute temperature (K), electronic and lattice thermal conductivity ($Wm^{-1}\ K^{-1}$), respectively [2, 3]. According to the above equation, the enhancement of TE performance is a challenging factor, due to the interdependency among thermoelectric properties. The effective way to enhance the zT value is to reduce the lattice thermal conductivity which is independent of other TE properties. Considerable reduction in lattice thermal conductivity of solid materials generally depends upon two categories such as extrinsic and intrinsic approaches. In extrinsic approaches, lattice vibration has occurred in phonon scatterings such as nanostructuring and all-scale hierarchical architecture [4–6], which sometimes introduce the scattering of carrier mobility and charge carrier. Contrarily, solid with intrinsically low lattice thermal conductivity have been obtained due to independent control over the electrical transport [7]. It has been achieved by layered structures with lattice anharmonicity [4], soft phonon modes [8], and liquid-like cation disordering in superionic substructures [9].

Among them, ternary silver bismuth sulfide ($AgBiS_2$) is an exceptional case that belongs to the I–V–VI_2 family of compounds (where I = Cu/Ag/Au; V = As/Sb/Bi; and VI = S/Se/Te). $AgBiS_2$ has two forms of crystal structure with respect to temperature such as (i) hexagonal phase with the space group *P-3m1* at room temperature, (ii) cubic phase with the space group of *Fm-3 m* at the temperatures above 473 K [9]. At high temperature, bulk-$AgBiS_2$ has possessed the disordered Ag and Bi atoms. The Bi element having $6s^2\ 6p^3$ valence electron configuration, in which $6p^3$ electrons are involved in the bond formation by chalcogens (S, Se and Te) and $6s^2$ electrons of Bi form a lone pair. Bi–X (X = S/Se/Te) bond has the electrostatic repulsion between the stereochemically active lone pair of Bi and the valence bonding charge of the chalcogen due to the origin of anharmonicity [10, 11]. Hence, the occurrence of strong anharmonicity in $AgBiS_2$ will be greater in comparison to its similar I–V–VI_2 group chalcogenide (Se_2/Te_2) as evidenced from the theoretical calculation of Grüneisen parameters [11]. The existence of disorder in the Ag/Bi positions and strong anharmonicity of Bi–S bond can expect low lattice thermal conductivity in cubic phases of $AgBiS_2$. Current researchers are focusing on the attractive and alternative of PbTe-based metal sulfides by the reason of toxicity of Pb and the extreme scantiness of Te [12]. Sulfur is 1000 times highly abundant than Te and has longer-term price stability & inexpensive [13, 14].

Furthermore, we expect low lattice thermal conductivity for the inclusion of antimony (Sb) into the cubic-$AgBiS_2$ and it is interesting to investigate the lattice thermal conductivity. Guan et al. [15] reported that the thermal conductivity of 0.33 W/mK at 773 K was prepared by ball-milled samples of 80% $Ag_{0.99}BiSe_2In_{0.01}$ + 20% $AgBiS_2$ composition. Guin et al. [16] reported that the low κ_{lat} of 0.4 − 0.5 $Wm^{-1}\ K^{-1}$ at 290–830 K range was obtained for $AgBiS_{1.92}Se_{0.08}$. Rathore et al. [17] reported that the lattice thermal conductivity of 0.68 W/mK at 298 K decreases to 0.48 W/mK at 820 K for cubic-$AgBiS_2$ (*n*-type) and it was prepared using vacuum sealing followed by spark plasma sintering process.

Multiphase materials reduce the thermal conductivity due to the different type of phonon scattering. Phonon scattering of the samples increase at interfaces, grain boundaries, and defects. In general, there are two types of boundaries that can influence the thermoelectric properties of polycrystalline thermoelectric materials. The first is the grain boundary of uniformly composed materials. Grain boundary engineering comprises altering grain size or shape to change the density of grain borders, as well as defect development at grain boundaries. The second one is phase boundary between two or more materials with differing compositions. The phase border is the separation between host materials.

In this article, a simple and efficient solvothermal approach has been developed to synthesize $AgBiS_2$ and $AgBi_{1-x}Sb_xS_2$ (x = 0.5 to 1) using polyethylene glycol (PEG) as the soft template. The pellet was compacted by spark plasma sintering. The results revealed a multiphase of metal sulfide with different percentages due to various concentration of Sb substitution on Bi-site. The low thermal conductivity was obtained in $AgBi_{0.5}Sb_{0.5}S_2$ sample, which covers the range of 0.26–0.21 $Wm^{-1}\ K^{-1}$ over the temperature range of 303–453 K due to bond anharmonicity, grain boundaries in nanoscale, and strong scattering by disordered cation sublattice.

2 Experimental procedure

2.1 Synthesis of $AgBiS_2$ and $AgBi_{1-x}Sb_xS_2$ (x = 0.5 to 1)

In a typical solvothermal reaction, 0.01 mol of silver nitrate ($AgNO_3$) and 0.01 mol of bismuth nitrate ($Bi(NO_3)_3.5H_2O$) were dissolved in 60 mL ethylene glycol ($C_2H_6O_2$—EG). Polyethylene glycol (0.1 mmol) was further added to the above precursor solution and kept at 40 °C for 4 h. Then, thiourea (0.08 mol) was added to it and the solution was transferred to a Teflon-lined stainless-steel autoclave of 100 mL capacity. The reaction temperature was kept at 180 °C for 48 h. After the reaction, precipitates were filtered and washed several times with ethanol and distilled water. The black color product was dried at 60 °C for 8 h (this sample is denoted as S1). The same synthesis procedure was repeated to prepare the samples S2–S4 by varying the concentration of $Bi(NO_3)_3.5H_2O$ with the addition of antimony chloride ($SbCl_3$). The detailed summary of samples preparation is tabulated in Table 1.

The formation of materials was influenced by ionic radius and oxidation state of ions in the precursor solution. Herein the ionic radii of Bi^{3+}, Sb^{3+} and Ag^{+} (117 pm, 90 pm and 129 pm) are different and these ions interacted with sulfur (S^{2-}) ion having 170 pm ionic radius. Due to various concentration of Sb^{3+} and Bi^{3+} ions, multiphases have been obtained for S2, S3 and S4 samples.

3 Characterization

The X-ray Diffractometer patterns of the samples were taken in Malvern Panalytical-MAERIS High-resolution benchtop X-ray diffraction with Cu K_α radiation (λ = 1.5406 Å). The scanning speed was 0.18° per minute and scanning angle was kept from 20° to 70°. Room temperature optical diffuse reflectance measurements were carried out via SHIMADZU UV–Vis–NIR spectrometer: 3600 PLUS. The instrument was equipped with an integrating sphere in which $BaSO_4$ was used as a 100% reflectance standard. X-ray photoelectron spectroscopy (XPS) was obtained using a ULVAC-PHI, Inc spectrometer: PH15000 in which Al-K_α radiation source was used with 1486 eV excitation energy. The ruptured surfaces of all the bulk samples by SPS were observed by Field emission scanning electron microscope (FE-SEM) (FEI Quanta 200F) at an accelerating voltage of 15 kV. Thermal analyses of all synthesized samples were carried out by (DTG-60A) thermal gravimetric analysis (TG) and differential thermal gravimetric analysis (DTA) for the experiment performed under argon atmosphere from room temperature to 869 K at a heating rate of 10 °C/min.

4 Thermoelectric measurements

Synthesized powder samples were consolidated in a 10 mm inner diameter graphite die by spark plasma sintering system (SPS-511S, Japan). In which, the samples were sintered at 473 K with the heating rate of 100 °C/min maintained for 10 min with 50 MPa uniaxial pressure. Total thermal conductivity (κ_{total}) of the samples were calculated using the formula $\kappa_{total} = D.C_p.\rho$, where D is the thermal diffusivity, C_p is specific heat capacity, and ρ is the density of the sample. The density of SPS'ed pellet was calculated and it is ~ 65% compared to the theoretical density for S1–S4. Thermal diffusivity (D) was carried out using the laser flash method (Netzsch, LFA467HT), while the specific heat capacity (C_p) was indirectly found using Pyroceram 9606 as a reference sample in the temperature range from 303 to 455 K. The density of the samples (ρ) was calculated by Archimedes method.

Table 1 Details of precursors used in synthesis process $AgBi_{1-x}Sb_xS_2$ (x = 0.5 to 1) materials

Sb-content (X)	Sample code	$AgNO_3$ (mol)	$Bi(NO_3)_3.5H_2O$ (mol)	$SbCl_3$ (mol)	Thiourea (mol)	PEG-template (mmol)
0	S1	0.01	0.01	0	0.08	0.1
0.5	S2	0.01	0.005	0.005	0.08	0.1
0.75	S3	0.01	0.0025	0.0075	0.08	0.1
1	S4	0.01	0	0.01	0.08	0.1

5 Results and discussion

5.1 Phase structural, microstructural and bandgap analysis

To detect the presence of multiphases, XRD analysis was performed on samples S1–S4 and the obtained XRD patterns were analyzed using the X'pert and FullProf software programs. Rietveld refinement of the samples S1–S4 is shown in Fig. 1 which confirmed the formation of cubic phase of $AgBiS_2$. The phase-fraction percentage was calculated by Rietveld refinement and the phase of cubic-$AgBiS_2$ is 100% for sample S1. The calculated lattice parameters for cubic-$AgBiS_2$ are $a = b = c = 5.691$ Å. For S2, it was calculated as 73.7% of cubic-$AgSbS_2$, 22.59% of rhombohedral-Ag_3SbS_3, and 3.71% of orthorhombic-Bi_2S_3. The calculated lattice parameters are $a = b = c = 5.656$ Å for cubic-$AgSbS_2$; $a = b = 11.059$ Å and $c = 8.714$ Å for rhombohedral-Ag_3SbS_3; and $a = 11.188$ Å, $b = 11.326$ Å, $c = 3.932$ Å for orthorhombic-Bi_2S_3 in sample S2.

Rietveld refinement precisely exhibited the multiphase formation of sample S3 (Fig. 1). The phase-fraction percentage was calculated as 33.59% of rhombohedtral-Ag_3SbS_3, 20.98% of monoclinic-Ag_3SbS_3, 20.27% of monoclinic-$AgBi_3S_5$, 17.20% of cubic-$AgSbS_2$, & 7.96% of orthorhombic-Bi_2S_3, respectively. The lattice parameters were calculated as follows. $a = b = 11.012$ Å, $c = 8.669$ Å for rhombohedtral-Ag_3SbS_3; $a = 7.058$ Å, $b = 16.363$ Å, $c = 6.235$ Å for monoclinic-Ag_3SbS_3; $a = 13.168$ Å, $b = 4.018$ Å, $c = 16.547$ Å for monoclinic-$AgBi_3S_5$; $a = b = c = 5.614$ Å for cubic-$AgSbS_2$; and $a = 11.198$ Å, $b = 11.291$ Å, $c = 3.983$ Å for orthorhombic-Bi_2S_3. The phase-fraction percentage of sample S4 was calculated and the mixed phase of rhombohedral-Ag_3SbS_3, monoclinic-$AgSbS_2$, orthorhombic-Sb_2S_3 & cubic-$AgSbS_2$ are 34.63%, 30.91%, 19.66% & 14.80% as shown in Fig. 1. The lattice parameters were calculated as follows. $a = b = 11.051$ Å, c = 8.716 Å for rhombohedral-Ag_3SbS_3; $a = 13.199$ Å, $b = 4.298$ Å, c = 13.123 Å for monoclinic-$AgSbS_2$; $a = 11.241$ Å, $b = 11.308$ Å, c = 3.841 Å for orthorhombic-Sb_2S_3 and $a = b = c = 5.597$ Å for cubic-$AgSbS_2$. These test accuracies for the phase-fraction prediction are also tabulated as Table 2.

XPS analysis was performed to measure the binding energy and various chemical states of bonded elements. Figures 2 and 3 show the XPS spectra of samples S1–S4 to analyze the valence states of the elements. Figure 2a exhibits the survey spectra in which predominant photoelectron lines of Ag 3d, Bi 4f, S 2p, O 1 s and Sb 3d states were observed. Figure 2b shows the core-level spectra of Ag 3d for the samples in which the peaks were obtained at 373.5 eV and 367.5 eV for S1, 373.2 eV and 367.2 eV for S2, 372.2 eV and 366.1 eV for S3, and 373.2 and 367.2 eV for S4 corresponding to Ag $3d_{3/2}$ and Ag $3d_{5/2}$, respectively. It exhibited the Ag^+ oxidation state [16]. The peak shift toward the lower binding energy for the samples S2, S3, and S4 were attributed to the presence of interfacial chemical interactions. It is due to the inclusion of antimony which initiates the secondary phase. Similarly, Ag 3d peak shift was reported in $AgBiS_{1.92}Se_{0.8}$ nanocrystals, which was due to the inclusion of Se element [16].

Figure 3 shows the core-level spectra of Bi 4f (S1–S3), S 2p (S1–S4) and Sb 3d (S2–S4) of the samples. The broadening peaks of Bi 4f core spectra peak could be deconvoluted. The deconvoluted peaks of Bi $4f_{5/2}$ of Bi-O, Bi^{3+} & Bi-S species for S1 were located at 164.1 eV, 163.4 eV & 163 eV, respectively [18–20]. Similarly, the deconvoluted binding energy of Bi $4f_{7/2}$ corresponding to Bi–O, Bi^{3+} and Bi–S species were located at 158.7 eV, 158.4 eV and 157.6 eV, respectively [18–20]. The evidence of Bi–S species was obtained in XRD results which show the secondary peaks (Fig. 1). The occurrence of binding energy for Bi–O species was observed due to surface oxygen reacts with the sample. Figure 3a shows the binding energy of S $2p_{1/2}$ and S $2p_{3/2}$ peaks of S^{2-} located at 160.9 eV and 160.2 eV [21], respectively. Bi 4f core-level spectra showed the interaction of Bi^{3+} peak and Bi–S interaction. For sample S2, the observed binding energies of 162.8 eV, 161.4 eV, 160.5 eV and 157.5 eV were assigned to Bi 4f $_{5/2}$, S $2p_{1/2}$, S $2p_{3/2}$, and Bi $4f_{7/2}$, respectively. The spin–orbit splitting of multiple Bi 4f peaks was observed as 5.3 eV which confirmed the oxidation states of Bi^{3+} [22]. Similarly, the spin–orbit splitting of S 2p was observed as 0.9 eV which confirmed the oxidation states of S^{2-} [23]. The Bi 4f and S 2p spectra for sample S3 were deconvoluted into six peaks. The obtained peaks at 162.7 eV, 157.3 eV and 159.5 eV were assigned to Bi^{3+} and other Bi^{3+} species [24, 25], whereas the peaks at 162 eV and 156.4 eV were assigned to metallic Bi [26], respectively. It was due to the presence of $AgBi_3S_5$ and Bi_2S_3 phase as evidenced by XRD (Fig. 1). Moreover, the binding energy of S $2p_{1/2}$ peak located at 161.4 eV suggests

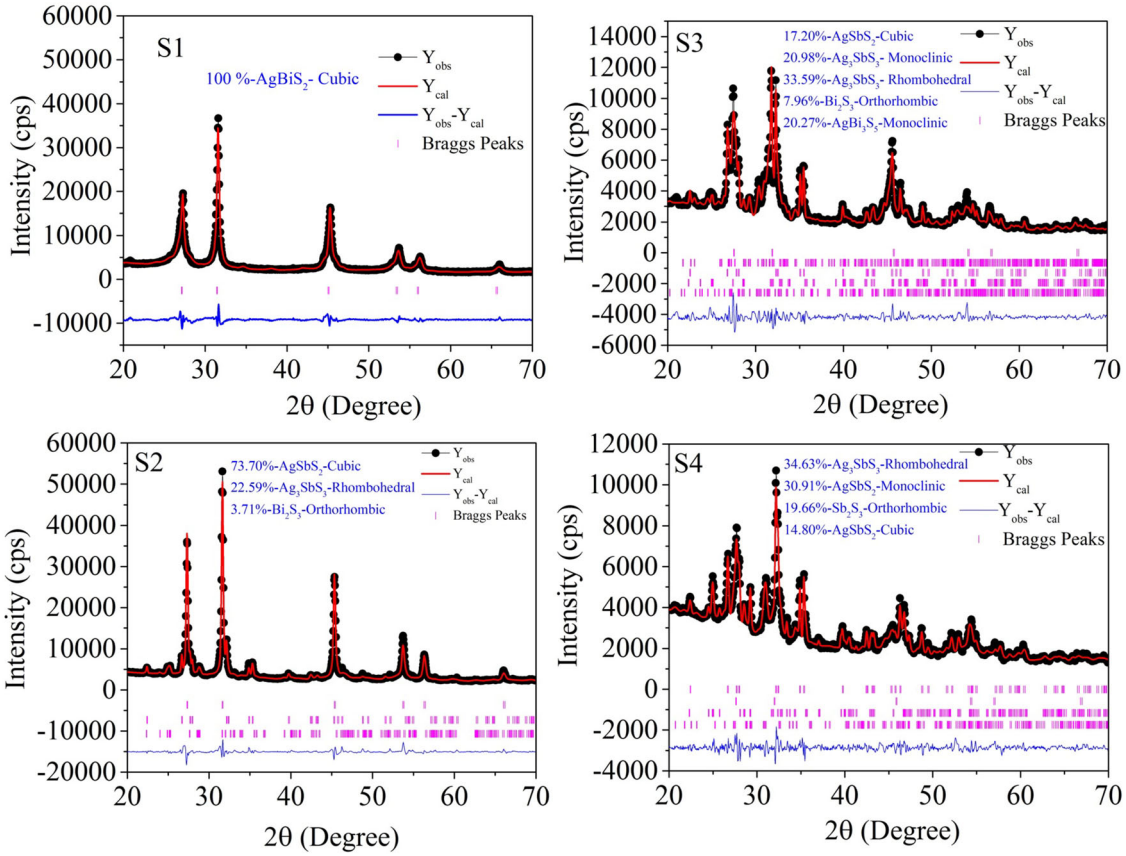

Fig. 1 Rietveld refinement results for sample S1–S4 ($AgBiS_2$ and $AgBi_{1-x}Sb_xS_2$ (x = 0–1) using Rietan-VENUS program, which deduce the mole ratio of the phases

Table 2 Compositions of samples measured by Rietveld refinement

Sample	Compositions
S1	$AgBiS_2$-Cubic (100%)
S2	$AgSbS_2$-Cubic (73.70%) + Ag_3SbS_3-Rhombohetral (22.59%) + Bi_2S_3-Orthorhombic (3.71%)
S3	Ag_3SbS_3-Rhombohetral (33.59%) + Ag_3SbS_3-Monoclinic (20.98%) + $AgBi_3S_5$-Monoclinic (20.27%) + $AgSbS_2$-Cubic (17.20%) + Bi_2S_3-Orthorhombic (7.96%)
S4	Ag_3SbS_3- Rhombohedral (34.63%) + $AgSbS_2$-Monoclinic (30.91%) + Sb_2S_3-Orthorhombic (19.66%) + $AgSbS_2$-Cubic (14.80%)

the existence of S^{2-} [27]. For sample S4, the resultant peak was deconvoluted into four peaks. The peaks at 160.8 eV and 163.1 eV were assigned to S^{2-}, whereas the peaks at 162.4 eV and 163.9 eV were assigned to S_2^{2-}, respectively [28, 29].

Figure 3b shows the core-level spectrum of Sb 3d for S2–S4 samples. The sample S2 exhibited the Sb 3d spectra, which could be deconvoluted into six peaks of Sb $3d_{5/2}$, Sb $3d_{3/2}$, and O 1 s as observed in Fig. 3b. It showed the peak for Sb^{3+} oxidation state of Sb $3d_{3/2}$ at a binding energy of 539.5 eV [30]. The characteristic peaks Sb $3d_{5/2}$ and Sb $3d_{3/2}$ were also observed at 528.8 eV and 538.1 eV, respectively. These peaks were attributed to the metal sulfide of Sb_2S_3, which was matched with the literature [31]. The peaks were obtained at binding energies of 532.3 eV, 530.2 eV, and 531.2 eV, which revealed that O 1 s and Sb $3d_{5/2}$ (Sb_2O_3) core level. These peaks were attributed to the surface oxygen adsorbed from the hydroxyl group present in the sample [32, 33].

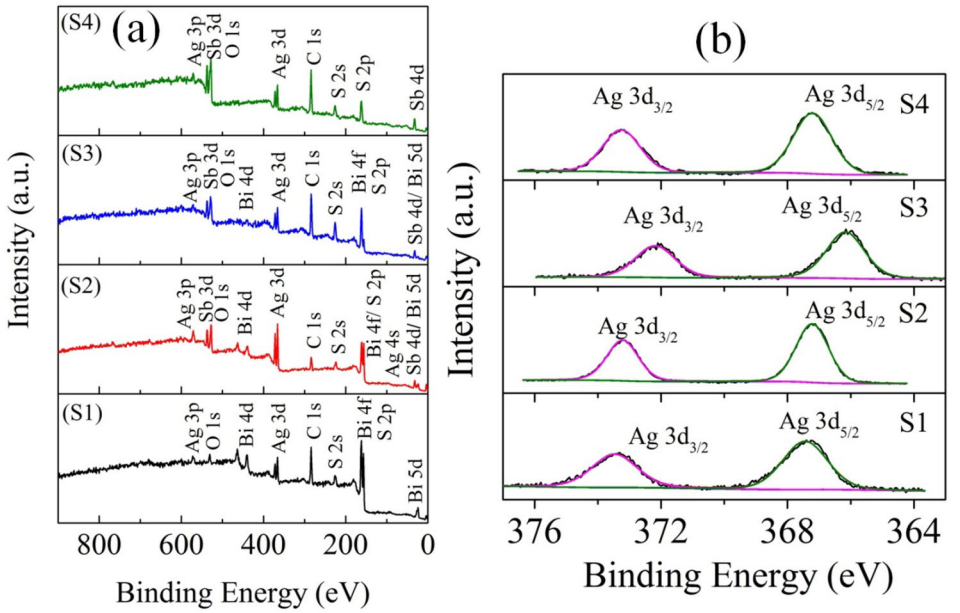

Fig. 2 Study of chemical states of the as-prepared powder of $AgBi_{1-x}Sb_xS_2$ (X = 0–1) solid solutions by XPS: **a** survey spectra, **b** photoelectron spectra of Ag 3d

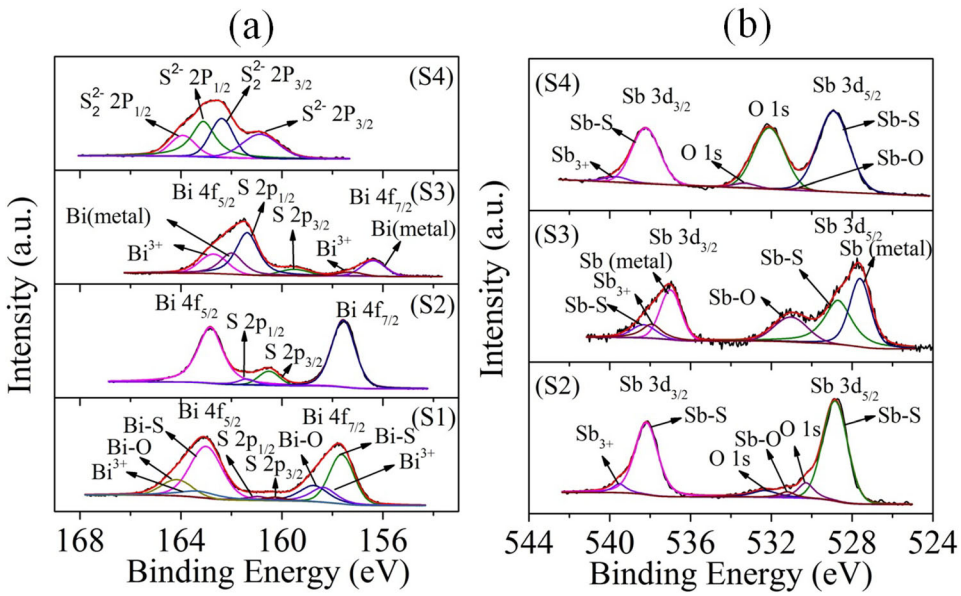

Fig. 3 Study of chemical states of the as-prepared powder of $AgBi_{1-x}Sb_xS_2$ (X = 0–1) solid solutions by XPS. **a** Photoelectron spectra of Bi 4f and S 2p. **b** Photoelectron spectra of Sb 3d and O 1s

Further, it showed the Sb^{3+} peak and Sb–S interaction, which confirmed the different phases of silver antimony sulfide ($AgSbS_2$, Ag_3SbS_3), as evidenced by the XRD result (Fig. 1). For sample S3, the broadened peaks were deconvoluted into six peaks obtained at the binding energy of 538.3 eV, 537.9 eV, 536.9 eV, 531.0 eV, 527.6 eV, and 528.7 eV as shown in Fig. 3b. In which, the binding energies of 538.3 eV, 528.7 eV, and 537.9 eV were attributed to various interactions for Sb_2S_3 confirming Sb^{3+} oxidation state [31, 34] . The binding energies of 536.9 eV, 527.6 eV, and 531 eV were attributed to the Sb $3d_{3/2}$, Sb $3d_{5/2}$ of metal Sb and chemisorbed oxygen species on the surface [28, 29, 32].

For sample S4, the observed peaks were deconvoluted into six peaks, which were centered at 539.7 eV, 538.2 eV, 533.3 eV, 532 eV, 528.9 eV, and 530.5 eV, respectively (Fig. 3b). In which, Sb $3d_{3/2}$, Sb $3d_{5/2}$ core of Sb_2S_3 (Sb–S species) and Sb^{3+} oxidation state of Sb $3d_{3/2}$ were centered at 538.2 eV, 528.9 eV, and 539.7 eV, respectively [31, 32]. Further, the binding energies of O 1s and Sb $3d_{3/2}$ of Sb_2O_3 were observed at 533.3 eV, 532 eV, and 530.5 eV, respectively, which

was due to the presence of oxygen from adsorption of water (hydroxyl group) [33, 35].

Thermal properties were analyzed by TG–DTA as shown in Fig. 4. For S1–S4, the weight loss occurred about 373 K–590 K which correspond to the evaporation of moisture and organic components from the samples [36, 37]. DTA plot displaying an endothermic peak at 453 K attributed to the phase transition of $AgBiS_2$ from β-phase to α-phase, which was stable at the temperature above 455 K (Sample S1) [38]. The endothermic peak appeared at 575 K was due to loss of SO_4 molecules [39]. For sample S2, the peak appeared at ~ 786 K which was attributed to the decomposition of $AgSbS_2$ [38]. The broad endothermic peaks obtained at ~ 640 K was attributed to the phase transition of monoclinic α-$AgSbS_2$ to cubic β-$AgSbS_2$ [38].

DTA plot displayed endothermic peak appeared at ~ 647 K which was attributed to the phase transition of monoclinic α-$AgSbS_2$ to cubic β-$AgSbS_2$ [38]. The endothermic broad peak obtained at ~ 410 K and ~ 793 K which is attributed to the high-temperature phase transition of orthorhombic-Bi_2S_3/$AgSbS_2$ to Ag_3SbS_3 and decomposition of $AgSbS_2$ [38, 39]. The strong endothermic peak obtained at 589 K which is due to decomposition of the sample S3. For sample S4, DTA showed the phase transition and strong decomposition of $AgSbS_2$ appeared at 660 K and 790 K, respectively [38]. The endothermic peak obtained ~ 733 K was attributed to the decomposition of $AgSbS_2$ into oxidation processes of Sb_2S_3 and Ag_2S [38]. In the TG–DTA graph, the decomposition started around 560 K for sample S1 and S2. Hence, the pellets were prepared at 473 K by spark plasma sintering method for thermoelectric measurements.

The surface micrographs of pelletized samples (S1-S4) are shown in Fig. 5a, which showed that the

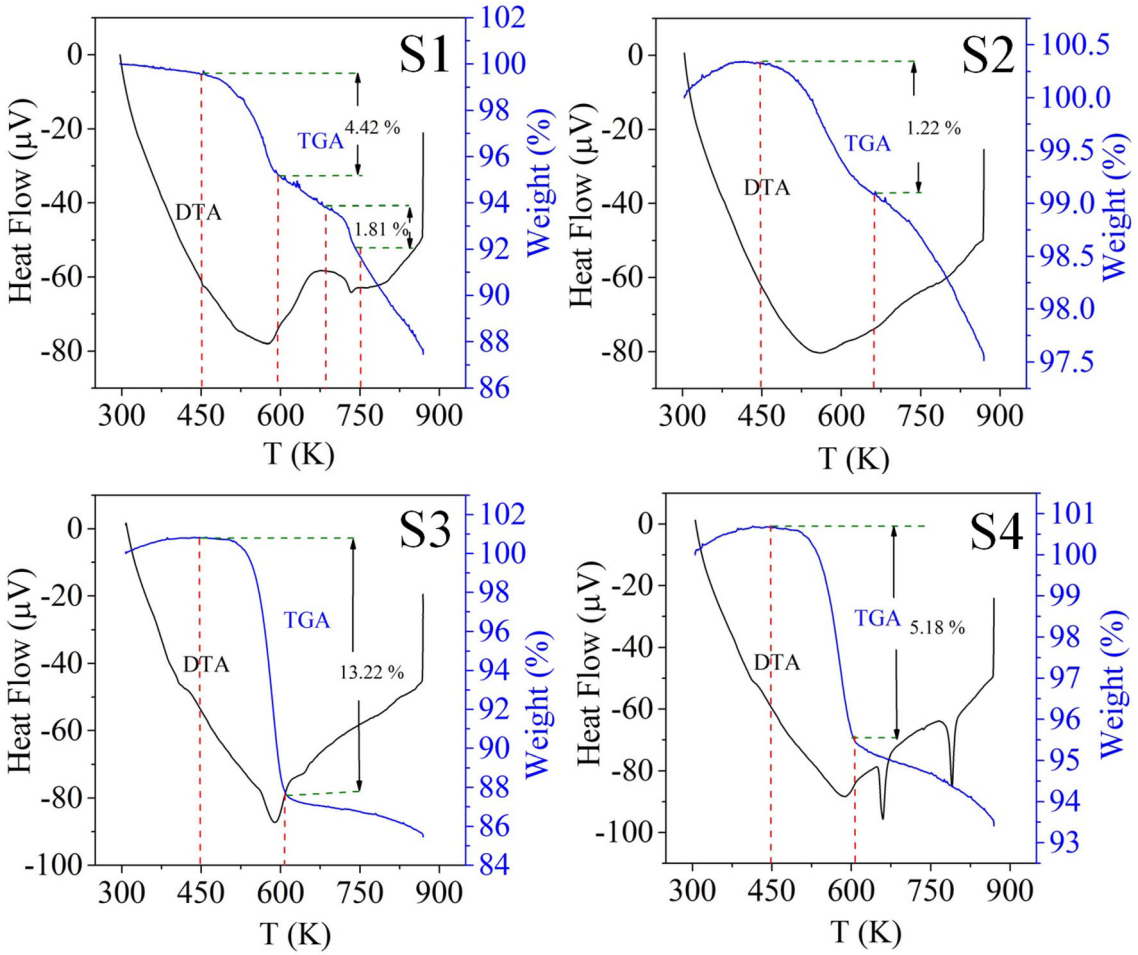

Fig. 4 TGA–DTA curve of $AgBi_{1-x}Sb_xS_2$ (0–1) from RT to 870 K

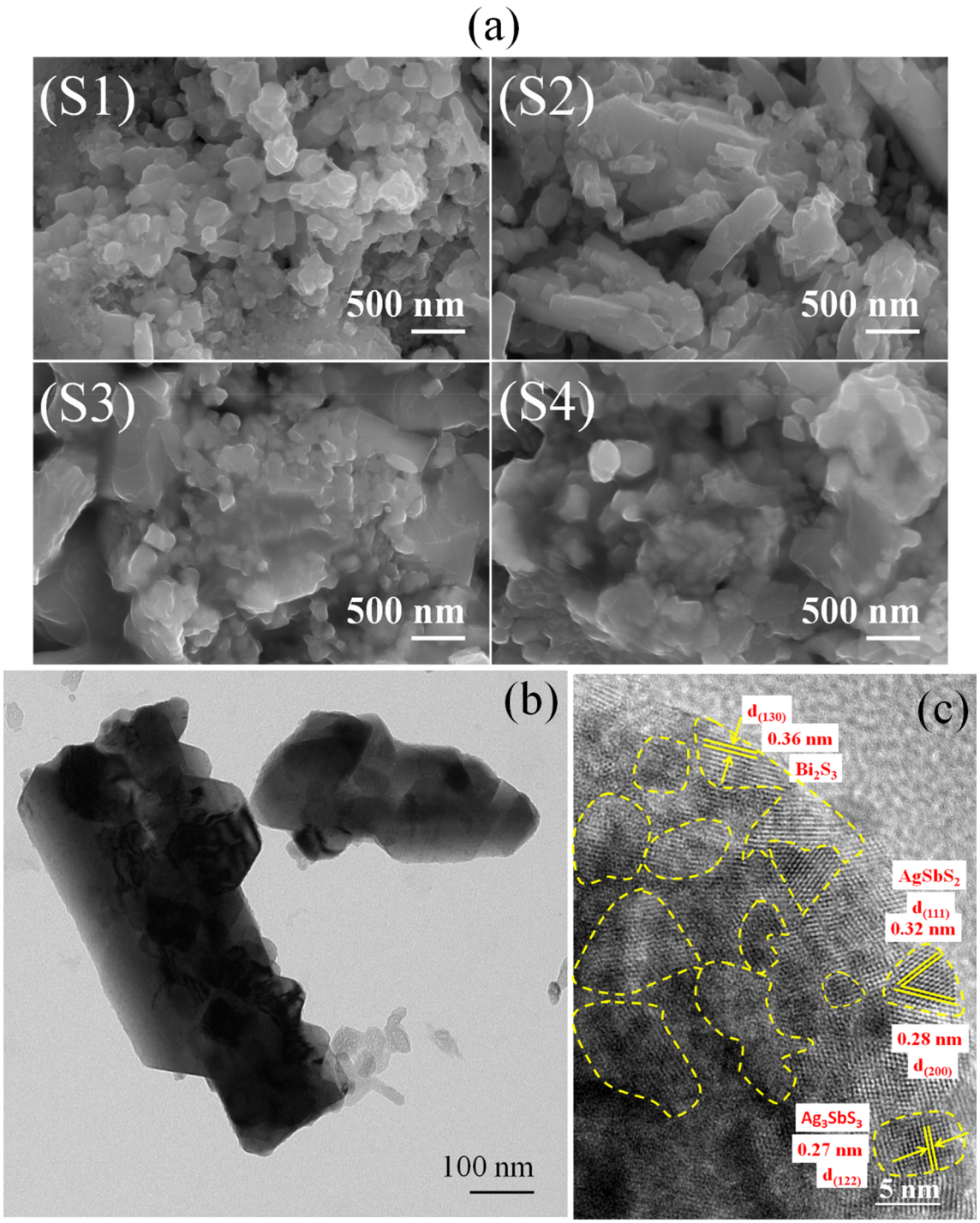

Fig. 5 **a** Cross-sectional HR-SEM of the bulk sample S1–S4 [$AgBi_{1-x}Sb_xS_2$ (x = 0–1)] **b** TEM for S2, and **c** HR-TEM micrograph for S2

cross-section of pellet was composed of densely packed nanoparticles. The morphology and the structure of the pellet sample S2 are further detected. Figure 5b displays TEM image of rectangular shape particles. The size of the rectangular rod-like morphology is ranging from 150 to 250 nm. The HR-TEM image (Fig. 5c) demonstrates that the inter-planar spacing values are 0.32 nm and 0.28 nm, corresponding to the d-spacing of the (1 1 1) and (2 0 0) planes of the cubic-$AgSbS_2$. In addition to that, the lattice fringes about 0.36 nm (1 3 0) for orthorhombic-Bi_2S_3 and 0.27 nm (1 2 2) for rhombohedral-Ag_3SbS_3

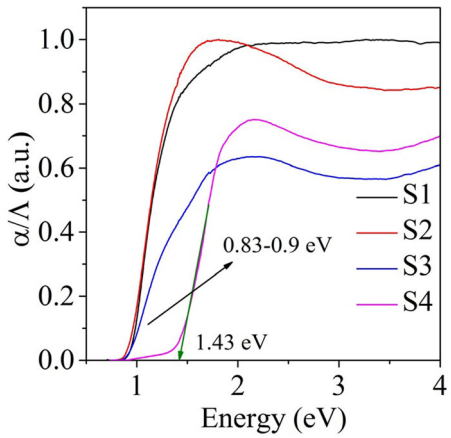

Fig. 6 Plot of $(\alpha hv)^2$ versus Energy (hv) of $AgBi_{1-x}Sb_xS_2$ $(x = 0–1)$

were also observed in sample S2. The HR-TEM exhibits the separation of grains with various structures and the random orientation of three different phases with large number of grain boundaries. It confirmed that the sample S2 had mixed phases of $AgSbS_2$, Ag_3SbS_3, and Bi_2S_3 polycrystalline compounds, which is in good agreement with XRD pattern shown in Fig. 1.

The absorption (α/Λ) data were calculated using Kubelka–Munk equation: $\alpha/\Lambda = (1 - R)^2/(2R)$ [40], where R is the reflectance, α and Λ are the absorption and scattering coefficient, respectively. The energy bandgap derived from α/Λ vs E_g (eV) plot is shown in Fig. 6. The experimental optical bandgaps were observed as 0.83–0.9 eV for S1–S3 and 1.43 eV for S4, respectively. The insignificant change in the bandgap values of sample S1–S3 were observed, but sample S4 (mixed phase of silver antimony sulfide) showed the bandgap value of 1.43 eV. All the samples showed direct bandgap semiconducting nature, which has the band edge close to the Fermi level.

The fundamental characterization of XRD and XPS results confirmed that the formation of multiphase with different fractional percentage may be due to the possibility of cationic and anionic interaction in precursor along with the corresponding concentration of Bi and Sb during synthesis process. The possibility of multiphase can be dependent on the quick availability of ionic interaction during the chemical synthesis due to the addition of Sb. So the multiphase materials with the different phase formation can tune the optical bandgap as shown in Fig. 6.

6 Thermoelectric properties

Figure 7a shows the thermal diffusivity as a function of temperature for all the samples. In which, Sb-substituted samples (S2–S4) show low diffusivity than sample S1 for the entire temperature range. At room temperature (303 K), thermal diffusivity of the samples were measured as 0.252 mm^2/s for S1, 0.166 mm^2/s for S2, 0.169 mm^2/S for S3, and 0.161 mm^2/s for S4, respectively. It confirmed that Sb substitution on Bi-site could create the defects in lattices which scatter the thermal carriers leading to low thermal conductivity. The defects might be attributed to the multiple phases present in the samples which were well consistent with XRD analysis. At 453 K, it showed the reduction of thermal diffusivity as 0.208 mm^2/s for S1, 0.14 mm^2/s for S2, 0.139 mm^2/s for S3, and 0.133 mm^2/s for S4, respectively. When increasing the temperature from 303 to 453 K, it was decreased by 17.5% for S1, 15.6% for S2, 17.75% for S3, and 17.4% for S4, respectively.

The specific heat capacity (C_p) of all the samples are shown in Fig. 7b in which it was measured as 0.418 J/gK for S1, 0.444 J/gK for S2, 0.583 J/gK for S3, and 0.499 J/gK for S4, respectively. It is noteworthy that, the trend of C_p curve was influenced by the phases present in the samples. The sample S3 showed increasing–decreasing trend occurring at 363 K–423 K, which can be possibly attributed to phases transition present in the samples. In specific, sample S1 has one phases and sample S2–S4 have more than two phases as tabulated in Table 2. It could be attributed to the phase transition which was evidenced from the DTA curve showing the endothermic peak over the temperature range of 370–406 K (Fig. 4).

Remarkably, λ type transition was observed in the temperature-dependent C_p in 363–423 K range (Fig. 7b), which confirmed the order–disorder type transition in sample S3. The κ_{total} values covered the range of 0.29–0.57 Wm^{-2} K^{-1} (Fig. 7c) over the temperature range of 303 to 453 K. Similar type of lambda transitions have been found in nanocrystalline $AgBiS_2$ [16], where cation rearrangement was responsible for the same [41]. A sharp peak in the κ_{total} occurs for the sample S3, which may be due to phase transition for $AgSbS_2$ to Ag_3SbS_3 in sample S3 which was consistent with DTA results. Figure 7c shows the low thermal conductivity for Sb included phase samples (S2) compared to the $AgBiS_2$ phase.

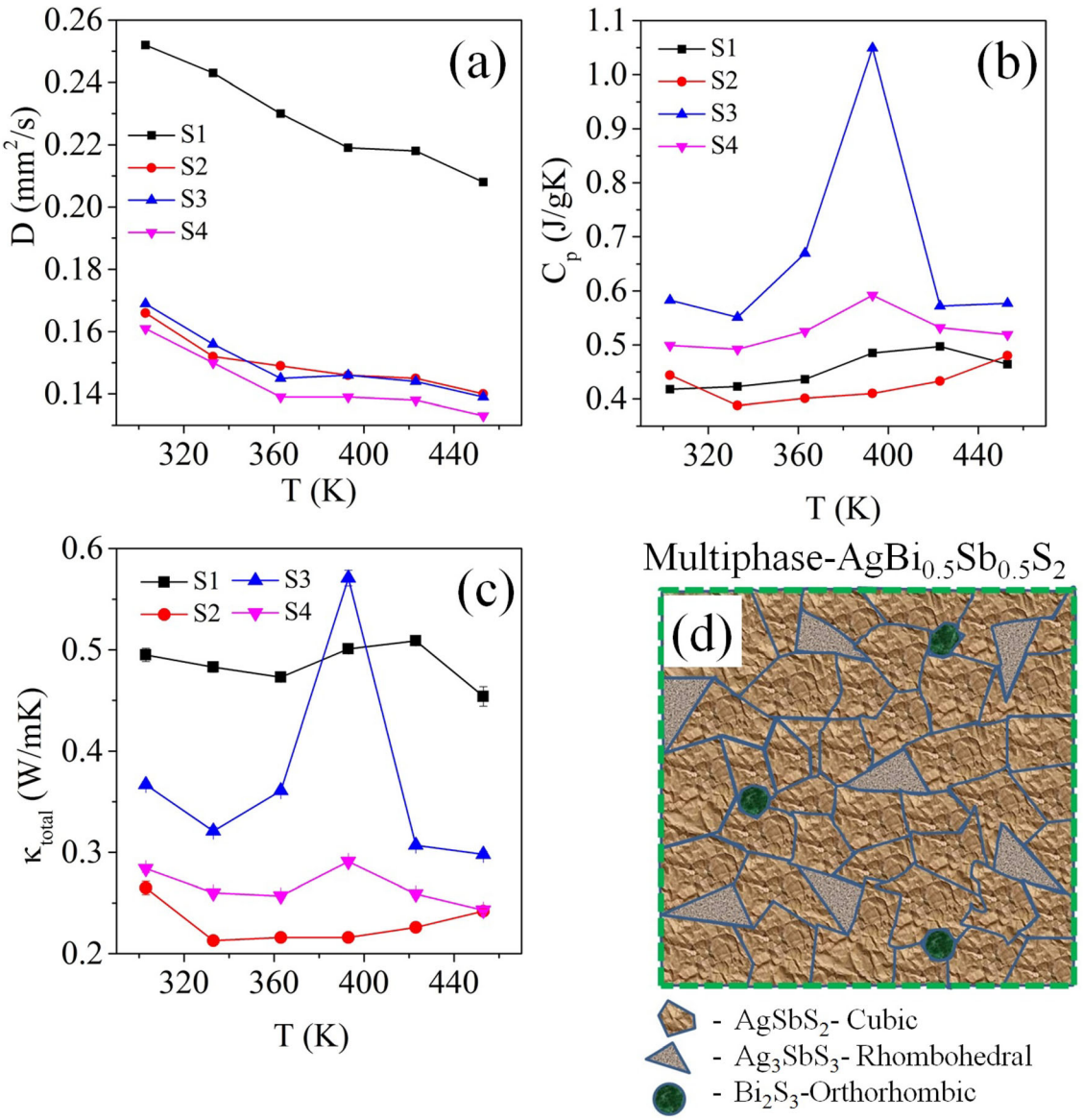

Fig. 7 Temperature dependence of **a** thermal diffusivity; **b** specific heat capacity; **c** thermal conductivity of $AgBi_{1-x}Sb_xS_2$ (x = 0–1) bulks. **d** Schematic illustration showing the existence of sample S2

The thermal conductivity of sample S2 is much lower than that of other samples. The measured results of thermal conductivity were compared with previous reports as shown in Fig. 8 which showed that Sb-substituted samples have low thermal conductivity than that of other reported values. Remarkably, sample S2 ($AgBi_{0.5}Sb_{0.5}S2$) exhibited low thermal conductivity of 0.213 Wm^{-1} K^{-1} at 333 K which was 50% decrement from nanocrystalline [16] and 68% decrement from bulk-$AgBiS_2$ [17], respectively. The reduction in thermal conductivity was plausibly predicted by significant scattering for heat carrying phonons. By which the phonons were scattered at grain boundaries due to multiple phases of cubic-$AgSbS_2$, rhombohedral-Ag_3SbS_3 and orthorhombic-Bi_2S_3 present in the samples. It reduced the thermal conductivity to a low level as 0.213 Wm^{-1} K^{-1} at 333 K for sample S2. The grain boundaries with different phases initiate the grain boundary scattering which reduces the thermal conductivity and different grain boundaries of the sample is clearly shown in HR-TEM results (Fig. 5c).

In single-phase material ($AgBiS_2$), the grain boundary scattering mechanism occurs primarily and

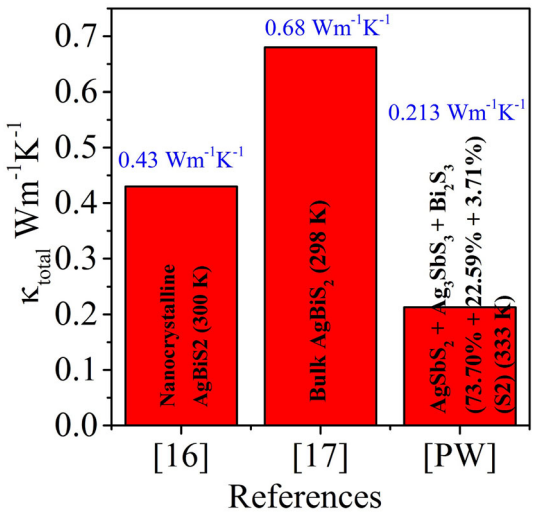

Fig. 8 Schematic diagram for comparison of thermoelectric properties with reports

it scatters the phonons having shorter wavelength. In multiphase materials (S2-S4), grain boundaries as well as phase boundaries play a vital role to scatter the phonons. This approach has the remarkable potential to reduce thermal conductivity through the introduction of Sb substitution in matrix (multiphase material). At the phase boundary, there are two main mechanisms for phonon scattering. (i) The strain induced by the slightly mismatched lattice which causes phonon scattering at a (semi)coherent boundary. This impact is reasonably comparable to point defects. (ii) The second mechanism is phonon scattering at an incoherent boundary. The mismatched phonon modes are the sources of the low thermal conductivity. In addition, the incoherent border serves as a carrier scattering centers [42].

Zhang et al. [43] reported that the presence of multi-nanophases has reduced the lattice thermal conductivity via phonon scattering and enhanced the power factor by incorporated multi-nanophases. The low thermal conductivity of the sample S2 was observed due to the following aspects such as (i) volume fraction of multiphases which depends on the shape and orientation of phases, (ii) crystallographic misorientation with the origin of grain size effect in polycrystalline materials, and (iii) the differential acoustic scattering due to the two phases (planar interface) [44]. The multiphase and polycrystalline behavior of cubic-$AgSbS_2$, rhombohedral-Ag_3SbS_3 and orthorhombic-Bi_2S_3 were clearly seen in HRTEM analysis. It is also represented schematically in Fig. 7d.

7 Conclusions

We have reported the experimental realization of less-toxic and abundant $AgBiS_2$ and $AgBi_{1-x}Sb_xS_2$ (x = 0.5–1) for mid-temperature thermoelectric energy harvesting application. The pristine & mixed phase of $AgBiS_2$ & $AgBi_{1-x}Sb_xS_2$ (x = 0.5–1) were synthesized using solvothermal followed by spark plasma sintering method. The material stability of the samples has been studied using TG–DTA measurements and the structural purity of the samples has been investigated using Rietveld refinement technique. The surface morphology showed a densely packed cross-sectional microstructure of pellet samples. The results revealed the significant and beneficial role of antimony-substituted multiphase sample S2 ($AgBi_{0.5}Sb_{0.5}S_2$) and the sample S2 has the presence of the multiphase of $AgSbS_2$ (73.70%), Ag_3SbS_3 (22.59%), and Bi_2S_3 (3.71%). The optical properties showed the narrow optical bandgap of ~ 0.83 eV–1.3 eV which was beneficial to good electrical transport. The bandgap variation with the nominal composition has been investigated. $AgBiS_2$ and $AgBi_{1-x}Sb_xS_2$ (x = 0.5–1) have numerous interfaces and grain boundaries due to the presence of multiphase in the samples. The grain boundaries are known as a disordered arrangement of atoms, which remarkably enhanced the phonon scattering. It led to the low thermal conductivity of 0.21 Wm^{-1} K^{-1} at 333 K in the sample S2. The plausible reason for low thermal conductivity was predicted as the phonon scattering mechanism at grain boundaries of multiphase present in the samples. This study provides opportunities for the design and tuning of the multiphase material and achieving physical properties tenability.

Acknowledgements

The authors would like to thank the "Nanotechnology Research Centre (NRC), SRM Institute of Science and Technology", for characterization facilities.

Author contributions

TM: methodology, investigation, visualization, writing—original draft, writing—review and editing. SK: conceptualization, visualization, writing—original draft, writing—review and editing, KK: conceptualization, data curation, supervision, resources, validation, funding acquisition, project administration. ESK: conceptualization, data curation, supervision, resources, validation, funding acquisition, project administration. MN: conceptualization, data curation, supervision, resources, validation, funding acquisition, project administration.

Data availability

The data presented in this study are available upon request from the corresponding author.

Declarations

Competing interest The authors declare that they have no known competing financial interests or personal relationships that could have appeared to influence the work reported in this paper.

References

1. B.I. Ismail, W.H. Ahmed, Thermoelectric power generation using waste-heat energy as an alternative green technology. Rec. Patent Electr. Eng. **2**, 27–39 (2009)
2. K. Nielsch, J. Bachmann, J. Kimling, H. Bottner, Thermoelectric nanostructures: from physical model systems towards nanograined composites. Adv. Energy Mater. **1**, 713–731 (2011)
3. J. He, T.M. Tritt, Advances in thermoelectric materials research: looking back and moving forward. Science **357**, 1367 (2017)
4. J. Li, J. Yang, B. Shi, W. Zhai, C. Zhang, Y. Yan, P. Liu, Ternary multicomponent Ba/Mg/Si compounds with inherent bonding hierarchy and rattling Ba atoms toward low lattice thermal conductivity. Phys. Chem. Chem. Phys. **22**, 18556–18561 (2020)
5. K. Biswas, J. He, Q. Zhang, G. Wang, C. Uher, V.P. Dravid, M.G. Kanatzidis, Strained endotaxial nanostructures with high thermoelectric figure of merit. Nat. Chem. **3**, 160–166 (2011)
6. K. Biswas, J. He, I.D. Blum, C.I. Wu, T.P. Hogan, D.N. Seidman, V.P. Dravid, M.G. Kanatzidis, High-performance bulk thermoelectrics with all-scale hierarchical architectures. Nature **489**, 414–418 (2012)
7. M.K. Jana, K. Biswas, Crystalline solids with intrinsically low lattice thermal conductivity for thermoelectric energy conversion. ACS Energy Lett **3**, 1315–1324 (2018)
8. M. Samanta, K. Pal, P. Pal, U.V. Waghmare, K. Biswas, Localized vibrations of Bi bilayer leading to ultralow lattice thermal conductivity and high thermoelectric performance in weak topological insulator n-type BiSe. J. Am. Chem. Soc. **140**, 5866–5872 (2018)
9. F. Tesfaye, D. Lindberg, Thermochemical properties of selected ternary phases in the Ag–Bi–S system. J. Mater. Sci. **51**, 5750–5759 (2016)
10. D.T. Morelli, V. Jovovic, J.P. Heremans, Intrinsically Minimal Thermal Conductivity in Cubic $I-V-VI_2$ Semiconductors. Phys. Rev. Lett. **101**, 035901 (2008)
11. M.D. Nielsen, V. Ozolins, J.P. Heremans, Lone pair electrons minimize lattice thermalconductivity. Energy Environ. Sci. **6**, 570–578 (2012)
12. P. Baláž, M. Achimovičová, M. Baláž, K. Chen, O. Dobrozhan, E. Guilmeau, J. Hejtmánek, K. Knížek, L. Kubíčková, P. Levinský, V. Puchý, M.J. Reece, P. Varga, R. Zhang, Thermoelectric Cu–S-based materials synthesized via a scalable mechanochemical process. ACS Sustain. Chem. Eng. **9**, 2003–2016 (2021)
13. Z. Hu, S. Gao, Upper crustal abundances of trace elements: a revision and update. Chem. Geol. **253**, 205–221 (2008)
14. M. Vázquez, E. Pallé, P. M. Rodríguez, The earth as a distant planet, The Earth in Time, (2010) 35–105.
15. Y. Guan, Y. Huang, D. Wu, D. Feng, M. He, J. He, Enhanced thermoelectric performance realized in $AgBiS_2$ composited $AgBiSe_2$ through indium doping and mechanical alloying. Appl. Phys. Lett. **112**, 213905 (2018)
16. S.N. Guin, K. Biswas, Cation disorder and bond anharmonicity optimize the thermoelectric properties in kinetically stabilized rocksalt $AgBiS_2$ nanocrystals. Chem. Mater. **25**, 3225–3231 (2013)
17. E. Rathore, R. Juneja, S.P. Culver, N. Minafra, A.K. Singh, W.G. Zeier, K. Biswas, Origin of ultra-low thermal conductivity in n-type cubic bulk $AgBiS_2$: soft Ag vibrations and local structural distortion induced by Bi $6s^2$ lone pair. Chem. Mater. **31**, 2106–2113 (2019)
18. A.K. Abay, D.H. Kuo, X. Chen, A.D. Saragih, A new V-doped $Bi_2(O, S)3$ oxysulfide catalyst for highly efficient catalytic reduction of 2-nitroaniline and organic dyes. Chemosphere **189**, 21–31 (2017)
19. S.V. Prabhakar Vattikuti, A.K. Reddy Police, J. Shim, C. Byon, In situ fabrication of the Bi_2O_3–V_2O_5 hybrid embedded with graphitic carbon nitride nanosheets: Oxygen vacancies mediated enhanced visible-light–driven

photocatalytic degradation of organic pollutants and hydrogen evolution. Appl. Surf. Sci. **447**, 740–756 (2018)
20. J. Zhou, G. Tian, Y. Chen, Y. Shi, C. Tian, K. Pan, H. Fu, Growth rate controlled synthesis of hierarchical Bi_2S_3/In_2S_3 core/shell microspheres with enhanced photocatalytic activity. Sci. Rep. **4**, 4027 (2014)
21. W.N. Kun, P.D. McNaughter, L.D. Nyamen, B.F. Spencer, P. O'Brien, P.T. Ndifon, N. Revaprasadu, Synthesis of $(Bi_{1-x}Sb_x)_2S_3$ solid solutions via thermal decomposition of bismuth and antimony piperidinedithiocarbamates. RSC Adv. **9**, 15836 (2019)
22. K. Tabatabaei, H. Lu, B.M. Nolan, X. Cen, C.E. McCold, X. Zhang, R.L. Brutchey, K.V. Benthem, J. Hihath, S.M. Kauzlarich, Bismuth doping of germanium nanocrystals through colloidal chemistry. Chem. Mater. **29**, 7353–7363 (2017)
23. K.V. Khot, S.S. Mali, N.B. Pawar, R.R. Kharade, R.M. Mane, V.V. Kondalkar, P.B. Patil, P.S. Patil, C.K. Hong, J.H. Kim, J. Heoe, P.N. Bhosale, Development of nanocoral-like Cd(SSe) thin films using an arrested precipitation technique and their application. New J. Chem. **38**, 5964–5974 (2014)
24. S. Ning, H. Lin, Y. Tong, X. Zhang, Q. Lin, Y. Zhang, J. Long, X. Wang, Dual couples Bi metal depositing and Ag@AgI islanding on BiOI 3D architectures for synergistic bactericidal mechanism of *E. coli* under visible light. Appl. Catal. B **204**, 1–10 (2017)
25. F. Ouyang, H. Li, Z. Gong, D. Pang, L. Qiu, Y. Wang, F. Dai, G. Cao, B. Bharti, Photocatalytic degradation of industrial acrylonitrile wastewater by F-S–Bi–TiO_2 catalyst of ultrafine nanoparticles dispersed with SiO2 under natural sunlight. Sci. Rep. **10**, 12379 (2020)
26. X. Li, Y. Sun, T. Xiong, G. Jiang, Y. Zhang, Z. Wu, F. Dong, Activation of amorphous bismuth oxide via plasmonic Bi metal for efficient visible-light photocatalysis. J. Catal. **352**, 102–112 (2017)
27. K.V. Khot, S.S. Mali, N.B. Pawar, R.R. Kharade, R.M. Mane, V.V. Kondalkar, P.B. Patil, P.S. Patil, C.K. Hong, J.H. Kim, J. Heo, P.N. Bhosale, Development of nanocoral-like Cd(SSe) thin films using an arrested precipitation technique and their application. New J. Chem. **38**, 5964–5974 (2014)
28. D. Escalera-Lópeza, Y. Niub, S.J. Park, M. Isaacs, K. Wilson, R.E. Palmerc, N.V. Reesa, Hydrogen evolution enhancement of ultra-low loading, size-selected molybdenum sulfide nanoclusters by sulfur enrichment. Appl. Catal. B **235**, 84–91 (2018)
29. D. Dinda, Md. Estak Ahmed, S. Mandal, B. Mondal, S.K. Saha, Amorphous molybdenum sulfide quantum dots: an efficient hydrogen evolution electrocatalyst in neutral medium. J. Mater. Chem. A **4**, 15486–15493 (2016)
30. M. Deng, S. Li, W. Hong, Y. Jiang, W. Xu, H. Shuai, H. Li, W. Wang, H. Hou, X. Ji, Natural stibnite ore (Sb_2S_3) embedded in sulfur doped carbon sheets: enhanced electrochemical properties as anode for sodium ions storage. RSC Adv. **9**, 15210–15216 (2019)
31. M.S. You, C.-S. Lim, D.H. Kwon, J.H. Heo, S.H. Im, K.J. Chae, Oxide-free Sb_2S_3 sensitized solar cells fabricated by spin and heat-treatment of Sb(III)(thioacetamide)$_2Cl_3$. Org. Electron. **21**, 155–159 (2015)
32. L. Bodenes, A. Darwiche, L. Monconduit, H. Martinez, The Solid Electrolyte Interphase a key parameter of the high performance of Sb in sodium-ion batteries: Comparative X-ray Photoelectron Spectroscopy study of Sb/Na-ion and Sb/Li-ion batteries. J. Power Sources **273**, 14–24 (2015)
33. L. Tan, A. Tang, Y. Zou, M. Long, Y. Zhang, J. Ouyang, J. Chen, Sb_2Se_3 assembling Sb_2O_3@ attapulgite as an emerging composites for catalytic hydrogenation of p-nitrophenol. Sci. Rep. **7**, 3281 (2017)
34. R. Jin, G. Chen, J. Pei, J. Sun, Y. Wang, Controllable synthesis and electrochemical hydrogen storage properties of Sb_2Se_3 ultralong nanobelts with urchin-like structures. Nanoscale **3**, 3893 (2011)
35. J. Li, K. Du, Y. Lai, Y. Chen, Z. Zhang, $ZnSb_2O_6$: an advanced anode material for Li-ion batteries. J. Mater. Chem. A **5**, 10843–10848 (2017)
36. S. Yin, Solution Processed Silver Sulfide Thin Films for Filament Memory Applications, Technical Report No. UCB/EECS-2010-166, University of California, Berkeley (2010).
37. M.A. Majeed Khan, S. Kumar, M. Ahamed, S.A. Alrokayan, M.S. AlSalhi, Structural and thermal studies of silver nanoparticles and electrical transport study of their thin films. Nanoscale Res. Lett. **6**, 434 (2011)
38. F. Tesfaye, D. Sukhomlinov, D. Lindberg, M. Moroz, P. Taskinen, L. Hupa, High-temperature oxidation of bismuth and antimony based sulfosalts. Miner. Process. Extr. M. **40**, 67–78 (2018)
39. K. Lukaszewicz, J. Stepien-Damm, A. Pietraszko, A. Kajokas, J. Grigas, Crystal structure, thermal expansion, dielectric permittivity and phase transitions of Bi_2S_3. Polish J. Chem. **73**, 541–546 (1999)
40. G. Tan, F. Shi, S. Hao, L.D. Zhao, H. Chi, X. Zhang, C. Uher, C. Wolverton, V.P. Dravid, M.G. Kanatzidis, Non-equilibrium processing leads to record highthermoelectric figure of merit in PbTe–SrTe. Nat. Commun. **7**, 12167 (2016)
41. C. Xiao, J. Xu, K. Li, J. Feng, J. Yang, Y. Xie, Superionic phase transition in silver chalcogenide nanocrystals realizing optimized thermoelectric performance. J. Am. Chem. Soc. **134**, 4287–4293 (2012)
42. H. Mun, S.M. Choi, K.H. Lee, S.W. Kim, Boundary engineering for the thermoelectric performance of bulk alloys based on bismuth telluride. ChemSusChem **8**, 2312–2326 (2015)

43. J. Zhang, D. Wu, D. He, D. Feng, M. Yin, X. Qin, J. He, Extraordinary thermoelectric performance realized in n-type PbTe through multiphase nanostructure engineering. Adv. Mater. **29**, 1703148 (2017)
44. A.M. Limarga, S. Shian, R.M. Leckie, C.G. Levi, D.R. Clarke, Thermal conductivity of single- and multi-phase compositions in the ZrO_2–Y_2O_3–Ta_2O_5 system. J. Eur. Ceram. Soc. **34**, 3085–3094 (2014)